ANALYSIS OF HYBRID ELECTROTHERMOMECHANICAL MICROACTUATORS WITH INTEGRATED ELECTROTHERMAL AND ELECTROSTATIC ACTUATION

BY

ARAVIND ALWAN

THESIS

Submitted in partial fulfillment of the requirements
for the degree of Master of Science in Mechanical Engineering
in the Graduate College of the
University of Illinois at Urbana-Champaign, 2011

Urbana, Illinois

Adviser:

Professor Narayana R. Aluru

Abstract

The goal of this research is to integrate electrothermal and electrostatic actuation in microelectromechanical systems (MEMS). We look at cases where these two types of actuation are intimately coupled and argue that such integrated electrothermomechanical microactuators have more advantages than pure electrothermal or electrostatic devices. We further propose a framework to model hybrid electrothermomechanical actuation to get a consistent solution for the coupled mechanical, thermal and electrical fields in the steady-state. Employing a Lagrangian approach, the inhomogeneous current conduction equation is used to describe the electric potential, while the thermal and displacement fields are obtained by solving the nonlinear heat conduction equation and by performing a large deformation mechanical analysis, respectively. To preserve numerical accuracy and reduce computational time, we also incorporate a boundary integral formulation to describe the electric potential in the medium surrounding the actuator. We show through the example of a hybrid double-beam actuator, that electrothermomechanical actuation results in low voltage, low power operation that could be used for switching applications in MEMS. We also extend the same device towards bidirectional actuation and demonstrate how it may be used to overcome common problems like stiction that occur in MEMS switches.

Acknowledgments

I would like to thank my adviser Prof. N. R. Aluru for all the help and guidance he has provided me in my research. Working with a large research group, I am amazed at how he still finds time for regular meetings and is always ready to lend an attentive ear to the problems I face. He has always urged me to pursue challenging problems and I am glad that his encouragement motivated me to work harder towards my goal.

I would also like to express my sincere gratitude to the faculty members present on my Ph.D. qualifying exam committee, Prof. Brian Thomas, Prof. Srinivasa Salapaka and Prof. Carlos Pantano-Rubino. They provided useful feedback about my research work. The discussion I had with them gave me a new understanding and appreciation for my work.

I would be remiss to not mention my colleagues in Prof. Aluru's research group. In addition to the countless engaging discussions that we had, I also cherish the many memorable activities that we were a part of, from playing softball to celebrating each other's accomplishments.

I also indebted to my friends in Champaign and family who have consistently supported me during every step of my life. The many wonderful years I have spent with them have continuously energized me and helped me maintain my focus on my work. I would have found it impossible to be where I am without their care and affection.

This work is supported in part by the National Science Foundation under grant number 0601479, in part by the Defense Advanced Research Projects Agency (DARPA) / Defense Sciences Office (DSO) and in part by the Department of Energy (DOE).

Credits

Table of Contents

List of Figures

Chapter 1

Introduction

Over the years, microelectromechanical systems (MEMS) have gained popularity in their use as transducers, both for sensing as well as for providing actuation. Their small size and relative low cost of fabrication makes them attractive alternatives to macroscale devices. In many cases, their performance is comparable to and even exceeds that of previously available technology. These advantages have fuelled a lot of research in this field to increase the efficiency and reliability of these devices. In addition to developing innovative ideas for novel transducers, research has also focussed on developing accurate numerical models for these devices in an effort to reliably predict the performance.

In this work, we limit our focus to microactuators that are used to produce displacement or mechanical force at small scales. Microactuators are used in a wide variety of applications, the most notable among them, being their use in micromechanical switches, which find their way into electronic circuits used in consumer electronics devices like cellphones and laptop computers. Given their widespread use, a lot of research has been done in this field, leading to the development of two major modes of actuation that are popular in the industry - electrothermal actuation and electrostatic actuation. The goal of this work is to identify the relative advantages and disadvantages of these two modes of actuation and to try to model situations where they may be used in conjunction with each other.

1.1 Motivation

Microctuators are employed in MEMS to produce mechanical motion. Electrothermal and electrostatic microactuators are two types of actuation mechanisms that are widely used in MEMS. Both these classes of actuators perform the same basic function of utilizing electrical energy to produce motion and/or mechanical force; however, they have very different characteristics.

Electrothermally actuated compliant microactuators or electro-thermal-compliant (ETC) microactuators [1] are popular because they can be easily fabricated using existing silicon microfabrication technology. ETC microactuators can operate at small drive voltages and are ideally suited for applications that demand

[1] © 2009 IEEE. Reprinted, with permission from A. Alwan and N. R. Aluru, Analysis of hybrid electrothermomechanical microactuators with integrated electrothermal and electrostatic actuation, Journal of Microelectromechanical Systems, Oct 2009.

relatively high output forces [2]. However, these actuators consume a lot of power [3] and are not the best choice for applications like MEMS switches, where it is required to maintain the deflected (ON) state for significant periods of time.

On the other hand, electrostatic actuators have the advantage of low power consumption [4], but when compared to ETC microactuators of similar dimensions the output force is almost 3 orders of magnitude lower, even with 10 times the drive voltage [2]. For devices that demand structures with relatively stiffer mechanical parts, this creates a problem because it becomes increasingly difficult to obtain the same displacement using voltages that lie within the CMOS operating regime. Moreover, the use of large voltages reduces device lifetime due to unwanted side-effects like dielectric charging [5].

By merging these two classes of actuators, it is possible to produce hybrid actuation schemes that combine the advantages of the two, namely, low power consumption and high output force. One such attempt to integrate electrothermal and electrostatic actuators in MEMS switches has been presented in [3]. This approach first employs a bimorph-type electrothermal actuator to bring the switch contacts near each other and then switches to electrostatic actuation to close the contacts and to hold the switch in the ON state. The resulting device operates on a small electrothermal drive voltage and uses electrostatic force only as a latching mechanism for standby operation. Work has also been done in integrating electrostatic and electromagnetic actuation [6] in relays to achieve similar benefits of low voltage and power consumption.

When designing hybrid electrothermomechanical (ETM) actuators, it is necessary to accurately model the interaction between different physical fields like mechanical, electrostatics, thermal and electrical. One main concern is that the electric fields that are generated during electrothermal as well as electrostatic actuation are not independent of each other. Obtaining a consistent solution requires a model that accounts for the interaction between the two. Although it is possible to circumvent this issue by separating the two actuation mechanisms spatially and/or temporally as done in [3], the optimal approach is to be able to model the situation where these may be applied simultaneously. In this work, we propose a model for a hybrid actuation mechanism that can use both electrothermal and electrostatic actuation at the same time. We demonstrate through numerical examples that hybrid actuation improves efficiency by achieving the same displacement using smaller drive voltages than those needed for either mechanism acting alone. In addition, it also retains the advantage of completely switching to electrostatic actuation for low power standby operation in the case of applications like MEMS switches.

1.2 Organization

This thesis is organised as follows: In Chapter 2 we develop a model for hybrid ETM actuators based on known electrothermal and electrostatic actuator models. We discuss separately the systems of equations that govern the behaviour of the electrical, thermal and mechanical fields that are involved in the modeling of ETM microactuators. We then describe the numerical method used to transform the continuum equations into a system of nonlinear equations described on the discretized domain.

Chapter 3 presents a few numerical examples to demonstrate the capabilities of the method proposed. After describing the simulation details like device-specific assumptions and material parameters, we look at the displacement characteristics of a specific example of an ETM microactuator vis-a-vis electrothermal and electrostatic microactuators. A simplified model of this microactuator is constructed to gain better physical insight into the device behaviour. We then talk about one of the novel features of the ETM actuator; that there exists a potential gradient within the actuator electrode, and discuss its implications. We also present a novel bidirectional microactuator design, which has been simulated using the proposed formulation. We finally conclude the discussion in Chapter 4 and present a summary of findings.

Chapter 2

Theory of hybrid ETM actuators

The hybrid ETM actuator employs a combination of electrothermal and electrostatic actuation mechanisms, and hence necessitates a multiphysics analysis of coupled electrical, thermal and mechanical domains. It is important to note that the electric field that causes thermal expansion and the electric field that generates electrostatic force are related. From the discussion that follows, we shall see why this coupling between the two cannot be accounted for by merely considering a superposition of the two effects.

A simple example demonstrating the hybrid microactuator principle can be constructed by considering the well-known Guckel double-beam electrothermal actuator [7] near a ground plate and applying a potential difference between the two, as shown in Figure 2.1. The classical Guckel actuator, shown in the figure as the double-beam structure, consists of two beams of equal length, one of which is thicker than the other. It is constructed using an isotropic material with a finite value of electrical conductivity. When the potential difference V_a is applied across its terminals, it causes asymmetric *Joule heating* and hence, unequal expansion in the two arms. By considering the two arms as a pair of resistors in series, it is easy to see that the electrical power dissipated in each of them is proportional to the resistance, which is greater for the thin beam due to its smaller area of cross-section. As a result, the thin beam becomes hotter and expands more, causing the device to bend [8], as shown in Figure 2.1.

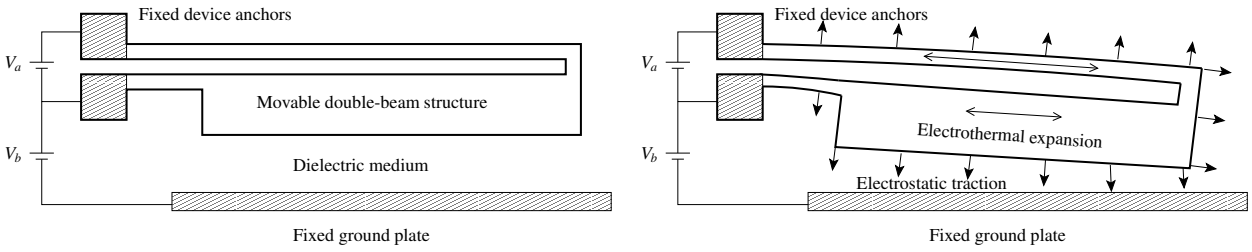

Figure 2.1: Schematic of the hybrid ETM actuator showing its constituent parts on the left and the different forces and boundary conditions acting on the device in the deformed configuration, on the right.

By applying another potential difference V_b between the double-beam structure and the ground plate as shown in Figure 2.1, we set up an electric field not only inside the double-beam, but also in the medium between the two electrodes. This leads to the development of a surface charge on the interfaces between the electrodes and the dielectric medium, resulting in an electrostatic traction that causes the electrodes

to deform. It is important to note that the electric field in the region changes as a result of motion of the electrodes, causing the surface charge to redistribute as well. Therefore, we look for a self-consistent solution of the electrical, thermal and displacement fields in the equilibrium state.

2.1 Governing equations

2.1.1 Mechanical analysis

Consider the problem domain shown in Figure 2.2. Under the action of electrothermal and electrostatic forces, the mechanical structure deforms until it attains equilibrium in a new configuration. Here, we are interested only in this final deformed configuration of the actuator and hence, we shall neglect all transient effects to simplify the analysis. As seen from the figure, we restrict the analysis to two dimensions for simplicity, although this analysis can easily be extended to three dimensions without too much additional effort. Let ω_1 denote the double beam structure, ω_2 the ground plate and $\overline{\omega}$ the domain exterior to these two in this final configuration. It is evident that for static equilibrium, all the governing equations for the actuator need to be satisfied in the final configuration. Since the problem domain obviously changes as a result of mechanical motion, we define a fixed reference configuration corresponding to the initial state, denoted by Ω_1, Ω_2 and $\overline{\Omega}$ and map the current configuration to it through the deformation gradient $\boldsymbol{F}$. Using this framework, we can develop a full Lagrangian scheme to express all equations in terms of quantities in the reference configuration.

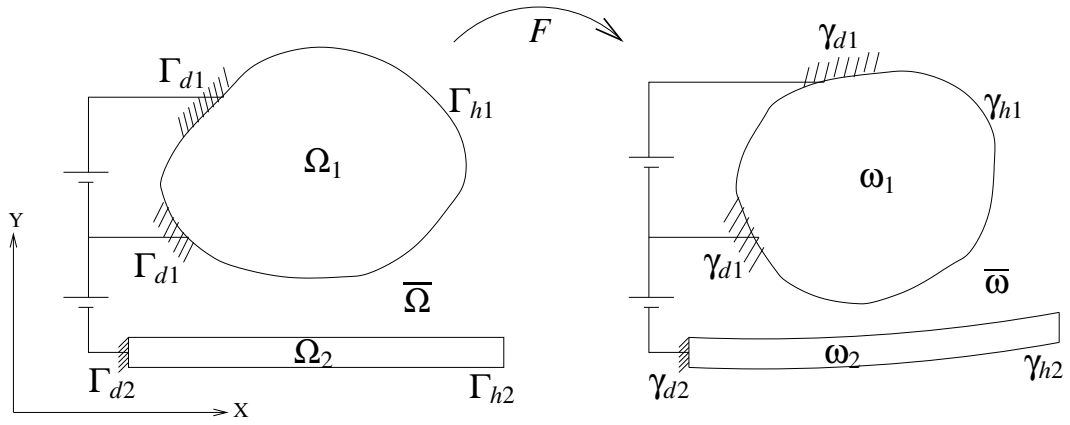

Figure 2.2: Generic problem domain for hybrid electrothermomechanical analysis. The initial, undeformed domain is on the left while the domain in the deformed configuration is shown on the right.

To obtain the mechanical deformation of the actuator, we perform 2D geometrically nonlinear analysis on the structure. The governing equations for the mechanical deformation of the electrodes, are given by [9],

$$\nabla \cdot (\boldsymbol{F}\boldsymbol{S}) = 0 \text{ in } \Omega_1, \Omega_2, \tag{2.1}$$

$$\boldsymbol{u} = \boldsymbol{u_0} \text{ on } \Gamma_d, \tag{2.2}$$

$$\boldsymbol{P}\boldsymbol{N} = \boldsymbol{H} \text{ on } \Gamma_h, \tag{2.3}$$

where $\boldsymbol{u}$ is the displacement vector, while $\boldsymbol{u_0}$ is the prescribed value of displacement on the part of the boundary, $\Gamma_d = \Gamma_{d1} \cup \Gamma_{d2}$, where a Dirichlet boundary condition is applied. Eq. (2.3) is the electrostatic traction boundary condition, which is applied on the rest of the boundary $\Gamma_h = \Gamma_{h1} \cup \Gamma_{h2}$. $\boldsymbol{F} = \boldsymbol{I} + \nabla \boldsymbol{u}$ is the deformation gradient and $\boldsymbol{S}$ is the second Piola-Kirchhoff stress tensor given by [10]

$$\boldsymbol{S} = \boldsymbol{C}\boldsymbol{E_s} - \frac{Y\alpha}{1-\nu}\Delta T \boldsymbol{I}, \tag{2.4}$$

where $\boldsymbol{C}$ is the material tensor, $\boldsymbol{E_s}$ is the Green-Lagrangian strain tensor, Y is the Young's modulus, α is the coefficient of thermal expansion, ν is the Poisson's ratio and $\boldsymbol{I}$ is the identity tensor. $\Delta T = T - T_0$ is the difference between the current temperature, T, and the reference temperature, T_0, at which thermal strains are assumed to be zero. In Equation (2.3), $\boldsymbol{P}$ is the first Piola-Kirchhoff stress tensor, $\boldsymbol{N}$ is the unit outward normal vector in the reference configuration and $\boldsymbol{H}$ is the surface traction vector that describes the electrostatic traction acting on the interfaces.

2.1.2 Thermal analysis

To compute the contribution to the stress tensor from thermal expansion, we need the temperature profile in the whole actuator. We assume that the temperature is constrained on Γ_d to some prescribed value T_0 (which, for simplicity, is taken to be equal to the reference temperature mentioned above) and convective heat transfer takes place on all the free surfaces, which include the side walls as well as the top and bottom surfaces of the device. The temperature field, T, is obtained by solving the heat conduction equation expressed in the reference configuration [10, 11],

$$\nabla \cdot \left(J\boldsymbol{F}^{-1}\boldsymbol{q_t}\right) = Q - \frac{h_{tb}}{t}\left(T - T_\infty\right) \text{ in } \Omega_1, \tag{2.5}$$

$$T = T_0 \text{ on } \Gamma_{d1}, \tag{2.6}$$

$$J\boldsymbol{F}^{-1}\boldsymbol{q_t} \cdot \boldsymbol{N} = h_s\left(T - T_\infty\right) \text{ on } \Gamma_{h1}, \tag{2.7}$$

where $J = det\boldsymbol{F}$ is the Jacobian of the deformation gradient and $\boldsymbol{q_t} = -k_t\boldsymbol{F}^{-T}\nabla T$ is the heat flux in the

body, k_t being the uniform, isotropic value of thermal conductivity for the material. Q is the heat supply per unit volume due to resistive Joule heating that is computed from the potential field, ϕ, as

$$Q = k_e \nabla\phi \cdot \nabla\phi, \tag{2.8}$$

where k_e is the uniform, isotropic value of electrical conductivity for the material. The terms h_{tb} and h_s in Equations (2.5) and (2.7), correspond to the coefficients of convective heat transfer from the top-bottom surfaces and the side walls of the body, respectively, while t is the thickness of the body in the Z-direction normal to the plane of the problem domain, T_∞ is the ambient temperature far away from the body and $\boldsymbol{N}$ is the unit outward normal vector on the boundary.

2.1.3 Electrical analysis

To complete the physical description of the problem, we need to compute the electric field that is responsible for the electrostatic traction as well as the Joule heating. In the classical electrothermal actuator, the electric field exists only inside the body of the actuator and is negligible elsewhere. One can compute this electric field, by solving the current conduction equation inside the body, along with appropriate boundary conditions on its surfaces [8]. On the other hand, in a purely electrostatic actuator, a potential gradient is established in the dielectric medium between two or more metallic electrodes. Since these electrodes may be approximated as ideal conductors, the electric field is practically zero in them and so their boundaries may be considered as equipotential surfaces. The electric field can then be computed by solving the Laplace equation for the potential in the dielectric medium surrounding the electrodes [12, 13, 14, 15].

As explained in the beginning of Chapter 2, in the hybrid ETM actuator, the electric field exists both inside the body of the actuator electrodes and in the medium outside. Returning to the two-electrode system shown in Figure 2.2, we note that the top electrode has a finite value of conductivity and a current flowing through it. Due to this current, the electric potential varies along the length of this electrode and hence, its boundary can no longer be considered as an equipotential surface. We see that the electric field in the medium between the electrodes differs from the pure electrostatic actuation case in that we can no longer merely solve the Laplace equation assuming ideal conductors. This calls for a new physical model that accurately describes the electric field in the entire region to correctly compute the thermal expansion in the body of actuator electrodes and the electrostatic traction on their surfaces.

For the purpose of the discussion here, we shall assume that the top electrode is made of an isotropic material with a uniform, finite value of electrical conductivity. The bottom ground plate is metallic and the entire device is placed in a dielectric medium. We assign a small fictitious value of electrical conductivity to

the dielectric medium. The electrical problem can then be modeled using the current conduction equation [16] by considering the entire domain as a region with a piecewise homogeneous value of conductivity. Let k_{e_1}, k_{e_2} and k_{e_0} denote the conductivities of the top electrode, the ground plate and the exterior region respectively. We apply a Dirichlet boundary condition by prescribing the electric potential on a part of the boundary denoted by Γ_d. Furthermore, we enfore continuity of potential and normal current density on the remaining part of the boundary denoted by Γ_h. The system of equations that describe the electric potential ϕ are:

$$\nabla \cdot \left(J\boldsymbol{F}^{-1} k_{e_1} \boldsymbol{F}^{-T} \nabla\phi \right) = 0 \text{ in } \Omega_1, \tag{2.9}$$

$$\nabla \cdot \left(J\boldsymbol{F}^{-1} k_{e_2} \boldsymbol{F}^{-T} \nabla\phi \right) = 0 \text{ in } \Omega_2, \tag{2.10}$$

$$\nabla \cdot \left(J\boldsymbol{F}^{-1} k_{e_0} \boldsymbol{F}^{-T} \nabla\phi \right) = 0 \text{ in } \overline{\Omega}, \tag{2.11}$$

$$\phi = \phi_0 \text{ on } \Gamma_d \tag{2.12}$$

$$\phi|_{\Omega_1} = \phi|_{\overline{\Omega}} \text{ on } \Gamma_h, \tag{2.13}$$

$$\left[J\boldsymbol{F}^{-1} k_{e_1} \boldsymbol{F}^{-T} \nabla\phi \cdot \boldsymbol{N} \right]_{\Omega_1} = \left[J\boldsymbol{F}^{-1} k_{e_0} \boldsymbol{F}^{-T} \nabla\phi \cdot \boldsymbol{N} \right]_{\overline{\Omega}} \text{ on } \Gamma_h, \tag{2.14}$$

where ϕ_0 is the prescribed potential.

It is immediately seen that since the electrical conductivity of the dielectric medium is a constant value, it can be taken outside the differential operator and Equation (2.11) for the exterior domain $\overline{\Omega}$ reduces to the familiar Laplace equation. Secondly, since the ground plate is metallic, the value of k_{e_2} is much higher than either k_{e_1} or k_{e_0}. Hence, the ground plate behaves like an ideal conductor with an equipotential surface. Since we know that the electric field is zero within an ideal conductor, we can avoid solving the current conduction equation inside Ω_2 and replace the interfacial boundary conditions on its surface with a Dirichlet boundary condition over the entire surface of the ground plate. Thirdly, it can be shown that in the limit where k_{e_0} goes to zero, the potential distribution approaches the true electrostatic potential.

Knowing the electric potential in the entire region, we can now compute the electrostatic traction term $\boldsymbol{H}$ on the electrode surfaces. When the potential difference is applied as shown in Figure 2.2, surface charges develop on all interfaces where there is discontinuity in either the electrical conductivity or dielectric permittivity. If we denote the normal current density as J_n and the dielectric permittivity as ϵ, the surface charge density and electrostatic traction at any general interface in the deformed configuration is given by [16]:

$$\sigma_s = J_n \left[\left. \frac{\epsilon}{k_e} \right|^+ - \left. \frac{\epsilon}{k_e} \right|^- \right], \tag{2.15}$$

$$\begin{aligned} \boldsymbol{f}_{es} &= \frac{1}{2}\,\sigma_s \left(\boldsymbol{E}|^- + \boldsymbol{E}|^+ \right) \\ &= \frac{1}{2}\,\sigma_s \left\{ \left(E_n|^- + E_n|^+ \right) \boldsymbol{n} + \left(E_t|^- + E_t|^+ \right) \boldsymbol{t} \right\} \\ &= \frac{1}{2}\,\sigma_s \left\{ \left(E_n|^- + E_n|^+ \right) \boldsymbol{n} + 2E_t|^- \boldsymbol{t} \right\}, \end{aligned} \tag{2.16}$$

where E_n and E_t are the components of the electric field, $\boldsymbol{E} = -\nabla\phi$, along the unit normal and tangential vectors in the deformed configuration, $\boldsymbol{n}$ and $\boldsymbol{t}$, respectively. The normal electric field is related to the normal current density through Ohm's law, $J_n = k_e|^- E_n|^- = k_e|^+ E_n|^+$. The $+/-$ signs are used to differentiate the electric fields and material properties of the media on either side of the interface; the $+$ sign being in the direction of the normal and the $-$ sign in the opposite direction. Conventionally, we assume that the normal vector at the surface is positive in the outward direction with respect to the body. As a result, the $-$ sign refers to the conducting material and the $+$ sign refers to the dielectric medium surrounding it. It is to be noted that in the last step of Equation (2.16), we have used the continuity of the tangential component of the electric field to express the electrostatic traction in terms of quantities that are known. In the limiting case when the conductivity goes to zero on one side of the interface e.g. along a metal-dielectric interface, these reduce to the usual expressions for σ_s and $\boldsymbol{f}_{es}$ in terms of the normal electric field, $\sigma_s = \epsilon E_n$ and $\boldsymbol{f}_{es} = [{\sigma_s}^2/(2\epsilon)]\boldsymbol{n}$. The electrostatic traction in the reference configuration can now be computed as,

$$\boldsymbol{H} = J \left| \boldsymbol{F}^{-T} \boldsymbol{N} \right| \boldsymbol{f}_{es}. \tag{2.17}$$

2.2 Numerical implementation

As discussed in Section 2.1, the analysis of hybrid ETM actuators involves three physical fields, namely mechanical, thermal and electrical. The equations describing these fields need to be satisfied in a self-consistent manner inside the actuator structure and, in the case of the electrical analysis, in the external region as well. This involves solving an exterior domain problem, which poses an additional challenge in that the problem domain is essentially an infinite one, because it has an open boundary. An efficient way to solve this problem involves transforming the equations describing the electrical field in the dielectric medium into boundary integral equations (BIEs) expressed over the boundary of the structure. BIE methods are popular in electrostatic analysis [17, 18] because of the reduction in computational cost achieved when discretizing

the boundary of the structure and solving the BIE over it, as opposed to solving the Laplace equation over the entire exterior region.

After formulating the problem as a BIE, the equations can be converted to discrete form so that they can be solved numerically. To solve the equations numerically, we discretized the actuator electrode domains using a finite element mesh and discretized the boundaries into a set of boundary elements. We then used a combination of finite element (FEM) and boundary element methods (BEM) to obtain the values of the physical fields at the nodes of the above mesh and in each of the boundary elements. We shall now see in detail how this numerical implementation is performed.

2.2.1 Boundary integral formulation

In the case of the hybrid ETM actuator, the electrical analysis involves solving the current conduction equations (Equations (2.9) - (2.11)) over the entire domain. However, as mentioned in the previous section, taking k_{e_0} outside the divergence operator in Equation (2.11), converts it into the Lagrangian form of the familiar Laplace equation. This motivates us to transform this equation to the boundary integral form, so that we can use a hybrid FEM/BEM approach [19, 20, 21, 22] to solve the electrical problem.

The boundary integral form of Equation (2.11) written in the reference configuration is given by,

$$\alpha(\boldsymbol{X})\phi(\boldsymbol{X}) = \int_\Gamma \phi(\boldsymbol{X'})\boldsymbol{F}^{-T}\nabla G(\boldsymbol{X},\boldsymbol{X'})\cdot\boldsymbol{F}^{-T}\boldsymbol{N'}\,J\,d\Gamma(\boldsymbol{X'}) + \int_\Gamma q_e(\boldsymbol{X'})G(\boldsymbol{X},\boldsymbol{X'})\,J\left|\boldsymbol{F}^{-T}\boldsymbol{N'}\right|\,d\Gamma(\boldsymbol{X'}) + \phi_{ref} \text{ on } \Gamma, \tag{2.18}$$

$$\int_\Gamma q_e(\boldsymbol{X'})\,J\left|\boldsymbol{F}^{-T}\boldsymbol{N'}\right|\,d\Gamma(\boldsymbol{X'}) = 0, \tag{2.19}$$

where $\boldsymbol{X}$ is the source point, $\boldsymbol{X'}$ is the field point, $G(\boldsymbol{X},\boldsymbol{X'})$ is the Green's function, $\boldsymbol{N'}$ is the unit outward normal vector at the field point $\boldsymbol{X'}$ in the Lagrangian frame and $q_e(\boldsymbol{x'}) = \partial\phi/\partial\boldsymbol{n'}$ is the flux at the field point $\boldsymbol{x'}$ in the Eulerian frame, $\boldsymbol{n'}$ being the corresponding unit outward normal at the same point. $\alpha(\boldsymbol{X})$ is the corner tensor, that is 1/2 for smooth boundaries [23]. For 2D problems, it can be shown that the Green's function is given by $G(\boldsymbol{X},\boldsymbol{X'}) = \ln|\boldsymbol{X}-\boldsymbol{X'}|/(2\pi)$, where $|\boldsymbol{X}-\boldsymbol{X'}|$ is the distance between the source point $\boldsymbol{X}$ and the field point $\boldsymbol{X'}$. The last term in Equation (2.18), ϕ_{ref}, is the unknown reference potential at a reference plane Γ_{ref} that is far away from the region of interest. With the introduction of this additional unknown ϕ_{ref}, we need an extra equation to solve the system. Equation (2.19) follows from the fact that the variation of potential on the reference plane is zero [17], i.e. $\boldsymbol{q_e}(\boldsymbol{X'}) = 0$ on Γ_{ref}.

2.2.2 Discretization of equations

To numerically solve the governing equations, we employ a coupled finite-element/boundary-element method using a Galerkin formulation to construct the weak form, which can then be easily solved. The mechanical and thermal equations are solved using FEM on their respective domains. For the electrical equations, we use FEM to solve Equation (2.9) for the electric potential in the domain and BEM to solve Equations (2.18) and (2.19) for the electric potential and the normal flux on the boundaries. To obtain a self-consistent solution between the mechanical, thermal and electrical fields, we use a staggered relaxation solver to cyclically solve for each of them until the change in the fields in a particular step dropped below some specified value of tolerance in error.

As seeen in Section 2.1.1, the displacement field is governed by Equations (2.1) - (2.3). This problem may be converted to the weak form, where we seek the equivalent solution $\boldsymbol{u}$ such that,

$$\int_{\Omega} \nabla\boldsymbol{\eta} : (\boldsymbol{F}\boldsymbol{S})\, d\Omega - \int_{\Gamma_h} \boldsymbol{\eta}\cdot\boldsymbol{H}\, d\Gamma = 0 \quad \forall\ \boldsymbol{\eta}\in\mathcal{V}, \tag{2.20}$$

where $\boldsymbol{\eta}$ is a test function chosen from the space of test functions, $\mathcal{H}$, given by,

$$\mathcal{H} = \left\{\boldsymbol{\eta} : \Omega \to \Re^2, \boldsymbol{\eta}|_{\Gamma_d} = \boldsymbol{0}\right\}. \tag{2.21}$$

Equation (2.20) may be solved using a standard Galerkin formulation, by approximating the solution using a set of nodal values on a finite element mesh (see [24] for details) to yield a nonlinear system of equations. We use a Newton-Raphson solver to iteratively solve the nonlinear system of equations to obtain the unknown nodal displacements. The next section gives details about using the Newton-Raphson method.

A similar procedure is adopted for the thermal equations given in Section 2.1.2. We first consider the weak form of the heat conduction equations in the deformed configuration, where we seek a temperature field, T, such that,

$$\begin{aligned}\int_{\Omega_1} \left(\boldsymbol{F}^{-T}\nabla w\right)\cdot\left(k_t\boldsymbol{F}^{-T}\nabla T\right) J\, d\Omega \;=\; & \int_{\Omega_1} w\left[Q - \frac{h_{tb}}{t}\left(T - T_\infty\right)\right] J\, d\Omega - \\ & \int_{\Gamma_{h1}} w h_s \left(T - T_\infty\right) J|\boldsymbol{F}^{-T}\boldsymbol{N}|\, d\Gamma,\end{aligned} \tag{2.22}$$

where w is a test function chosen from the space of test functions, $\mathcal{W}$, given by,

$$\mathcal{W} = \left\{w : \Omega \to \Re, w|_{\Gamma_{d1}} = 0\right\}. \tag{2.23}$$

To solve Equation (2.22), we first discretize the domain using a finite element mesh. Using a Bubnov-Galerkin method, we approximate both the solution field and the test function using a subspace of $\mathcal{W}$. In this subspace, both these functions are approximated as sums of nodal values (T_i and w_i respectively), weighted by the shape functions, ψ_i, where i is an index that goes from 1 to the number of nodes, n_d. Thus we construct approximations for T, w and their gradients as follows:

$$T \approx \sum_{1}^{n_d} \psi_i T_i, \quad w \approx \sum_{1}^{n_d} \psi_i w_i, \quad \nabla T \approx \sum_{1}^{n_d} B_i T_i, \quad \text{and} \quad \nabla w \approx \sum_{1}^{n_d} B_i w_i. \tag{2.24}$$

Substituting these into Equation (2.22), we get,

$$\int_{\Omega_1} \left[\sum_{i}^{n_d} B_i w_i\right] \boldsymbol{F}^{-1} k_t \boldsymbol{F}^{-T} \left[\sum_{j}^{n_d} B_j T_j\right] J \, d\Omega = \int_{\Omega_1} \left[\sum_{i}^{n_d} \psi_i w_i\right] \left[Q - \frac{h_{tb}}{t}\left\{\sum_{j}^{n_d} \psi_j T_j - T_\infty\right\}\right] J \, d\Omega - \int_{\Gamma_{h1}} \left[\sum_{i}^{n_d} \psi_i w_i\right] h_s \left[\sum_{j}^{n_d} \psi_j T_j - T_\infty\right] J |\boldsymbol{F}^{-T} \boldsymbol{N}| \, d\Gamma. \tag{2.25}$$

Since the above equation should hold for all possible values of w, we can rewrite Equation (2.25) as a system of equations for each value of $i = 1, 2, \ldots, n_d$,

$$\sum_{j}^{n_d} \left\{\int_{\Omega_1} \left[B_i \boldsymbol{F}^{-1} k_t \boldsymbol{F}^{-T} B_j + \psi_i \frac{h_{tb}}{t} \psi_j\right] J \, d\Omega + \int_{\Gamma_{h1}} \psi_i h_s \psi_j J |\boldsymbol{F}^{-T} \boldsymbol{N}| \, d\Gamma\right\} T_j = \int_{\Omega_1} \psi_i \left[Q + \frac{h_{tb}}{t} T_\infty\right] J \, d\Omega + \int_{\Gamma_{h1}} \psi_i h_s T_\infty J |\boldsymbol{F}^{-T} \boldsymbol{N}| \, d\Gamma. \tag{2.26}$$

In general, since k_t can be a function of temperature, Equation (2.26) represents a nonlinear system of equations. Such a system of equations can be solved using a nonlinear solver that utilizes the Newton-Raphson method.

The final set of equations to consider are those that describe the electrical field in the entire domain. This is governed by the current conduction equation in the actuator electrodes and in the region surrounding the electrodes. As discussed in Section 2.2.1, we replace Equation (2.11) with a boundary integral equation, which can be solved more accurately. Thus we separate the problem into two parts, where the first part comprises the equations that govern quantities in the actuator electrodes and the second part deals with the quantities in the exterior region, which are in turn described by quantities on the boundaries of the electrodes. By properly coupling these two parts, we get a consistent solution for the electric field everywhere. The coupling is achieved through continuity equations on the interfaces (Equations (2.13) and (2.14)).

We denote the potential and flux variables used in Equation (2.18) by $\tilde{\phi}$ and $\tilde{q}_e$ to distinguish them from those used in Equations (2.9) and (2.10). Transforming the latter equations to the weak form, we get,

$$\int_{\Omega} \left(\boldsymbol{F}^{-T} \nabla v \right) \cdot \left(k_e \boldsymbol{F}^{-T} \nabla \phi \right) J \, d\Omega = \int_{\Gamma_h} v k_{e_0} \tilde{q}_e J |\boldsymbol{F}^{-T} \boldsymbol{N}| \, d\Gamma, \tag{2.27}$$

where k_e is k_{e_1} for the top electrode and k_{e_2} for the bottom electrode respectively, and v is a test function chosen from the space of test functions, $\mathcal{V}$, given by,

$$\mathcal{V} = \{ v : \Omega \to \Re, v|_{\Gamma_d} = 0 \}. \tag{2.28}$$

Using the new definition of the variables on the boundary, the BIEs from Section 2.2.1 may now be written as,

$$\begin{aligned} \alpha(\boldsymbol{X}) \tilde{\phi}(\boldsymbol{X}) = & \int_{\Gamma} \tilde{\phi}(\boldsymbol{X'}) \boldsymbol{F}^{-T} \nabla G(\boldsymbol{X}, \boldsymbol{X'}) \cdot \boldsymbol{F}^{-T} \boldsymbol{N'} \, J \, d\Gamma(\boldsymbol{X'}) \\ & + \int_{\Gamma} \tilde{q}_e(\boldsymbol{X'}) G(\boldsymbol{X}, \boldsymbol{X'}) \, J \left| \boldsymbol{F}^{-T} \boldsymbol{N'} \right| \, d\Gamma(\boldsymbol{X'}) + \tilde{\phi}_{ref} \text{ on } \Gamma, \end{aligned} \tag{2.29}$$

$$\int_{\Gamma} \tilde{q}_e(\boldsymbol{X'}) \, J \left| \boldsymbol{F}^{-T} \boldsymbol{N'} \right| \, d\Gamma(\boldsymbol{X'}) = 0. \tag{2.30}$$

Noting that one of the interfacial continuity equation for the flux (Equation (2.14)) has already been incorporated into the weak form (Equation (2.27)) above, we complete the description of the problem by expressing the other continuity equation in integral form.

$$\int_{\Gamma_h} \left(\phi - \tilde{\phi} \right) J \left| \boldsymbol{F}^{-T} \boldsymbol{N'} \right| \, d\Gamma = 0. \tag{2.31}$$

The transformation of this set of equations to matrix form using the Galerkin method is very similar to that done for the thermal equations above. The only difference is that the finite element shape functions used to approximate the variables in the electrodes are different from those used on the boundary for the boundary elements. Proceeding as in the case of the thermal equations above, we can arrive at a linear system of equations, which can be solved to obtain the electrical field in the electrodes and on its boundary.

2.3 Solving the equations

In the previous section, we have seen how the governing equations for each of the analysis modes can be transformed into a system of equations, where the values of the field variables on nodes of the mesh are unknowns. If the resulting set of equations forms a linear system, then they may be directly converted to matrix form, which can then be solved using any direct solver. On the other hand, if the resulting equations are nonlinear, then we perform a linearization to obtain a linear system of equations. We then need to successively refine the solution until we obtain a proper convergence, to ensure that we have a consistent solution for the nodal parameters. The Newton-Raphson method is one such algorithm that is popularly used for solving nonlinear systems of equations.

Consider a nonlinear system of equations denoted by $\boldsymbol{R}(\boldsymbol{d})$, where $\boldsymbol{d}$ is the vector of nodal unknowns and $\boldsymbol{R}$ is the vector of residuals of the equations that comprise the nonlinear system. Our goal is to obtain the solution $\boldsymbol{d}^*$ such that $\boldsymbol{R}(\boldsymbol{d}^*)$ goes to zero. Assume that we start with some initial guess, $\boldsymbol{d}$, for the solution. We seek to obtain a better solution, $\boldsymbol{d}_{new}$, by correcting this guess with an increment $\Delta\boldsymbol{d}$, such that,

$$\boldsymbol{d}_\epsilon = \boldsymbol{d} + \epsilon\Delta\boldsymbol{d}, \tag{2.32}$$

where ϵ is a small tuning parameter and $\boldsymbol{d}_\epsilon$ is the corrected value. Since we want $\Delta\boldsymbol{d}$ to be such that the new residual after correction is close to zero, we perform a Taylor series expansion of $\boldsymbol{R}(\boldsymbol{d}_\epsilon)$ about $\epsilon = 0$ and truncate the expansion after the first order derivative. This is the linearization step, where we approximate the variation of $\boldsymbol{R}$ with $\boldsymbol{d}$ to be locally linear. Thus, we get,

$$\begin{aligned}\boldsymbol{R}(\boldsymbol{d}^*) = 0 \approx\ & \boldsymbol{R}(\boldsymbol{d}_\epsilon)|_{\epsilon=0} + \frac{d}{d\epsilon}\boldsymbol{R}(\boldsymbol{d}_\epsilon)\bigg|_{\epsilon=0}, \\ &= \boldsymbol{R}(\boldsymbol{d}) + \boldsymbol{K}\Delta\boldsymbol{d},\end{aligned} \tag{2.33}$$

where $\boldsymbol{K}$ is the derivative of the residual vector with respect to ϵ. Solving this matrix equation, we obtain the correction, $\Delta\boldsymbol{d}$, which is used to compute the new solution vector. The new solution vector is then used as the guess for the next linearization step as follows,

$$\boldsymbol{d} \leftarrow \boldsymbol{d} + \Delta\boldsymbol{d}. \tag{2.34}$$

This process is continued until the norm of the correction vector drops below some specified tolerance level. It can be shown that the Newton-Raphson method yields quadratic convergence in the solution as

long as the initial guess is not far from the solution. In practice, we can get a fairly accurate solution within a few iteration steps.

To solve the entire coupled problem, we employ a Newton-Raphson solver to solve the mechanical, thermal and electrical fields individually. In order to ensure that the coupling between the three fields has been captured accurately, we use a staggered relaxation solver that cyclically solves the above three problems until the changes in the values of each field drops below a specific tolerance level. A peculiar characteristic of this problem formulation is that the electromechanical coupling is known to introduce instabilities due to the pull-in phenomenon, which will be explained better in Section 3.2. This is due to the fact that the electrostatic force is nonlinear and increases as the electrodes come closer. Since we do not implement a mechanical contact model, there is no way to obtain a stable solution once the electrodes come into contact. To work around this problem, we constantly check if the solution converges uniformly. If a divergent solution is detected, then the iterative procedure is stopped and the simulation is labelled as having pulled-in. By updating the voltages in adequately small steps, it is possible to capture the point where the pull-in phenomenon sets in, with resonable accuracy.

Chapter 3

Numerical examples

Electromechanical microactuators convert electrical energy to mechanical displacement and/or force. The equilibrium or steady-state analysis of these actuators is performed by applying fixed voltages and observing the output displacement. In this chapter, we first describe the general simulation setup and device parameters that describe the actuators under consideration. We then attempt to illustrate the differences between the three actuator types mentioned in Chapter 2. We also examine the specific characteristics of the hybrid ETM actuator and how that is responsible for causing the difference in behaviour between the three actuator types. Finally we look at a more general type of actuator that generalizes the hybrid ETM actuator to achieve bidirectional actuation.

3.1 Simulation setup

The hybrid formulation developed in Chapter 2 can be used to simulate a wide variety of ETM actuator configurations. In this thesis, we shall concentrate on devices which have dimensions in the micrometer regime, where electrothermal and electrostatic actuation are roughly in the same order of magnitude so that the interplay of the two effects is most apparent. We shall assume that silicon is the principal material used to fabricate the devices and that its material properties are spatially uniform. The ground plate is made up of a material with a very high value of conductivity like aluminium, so that it can be assumed to behave like an ideal metal. The dielectric medium surrounding the electrodes is air.

The double-beam structure used in the examples has the same dimensions as device D4 mentioned in [8] with a ground plate placed at a distance of 2μm from the edge of the double beam structure as shown in Figure 3.1, such that it extends 17μm to either side of the thick beam in the horizontal direction. The device is oriented such that Figure 2.1 is the view from the top and the side walls correspond to the boundaries of the domain. The electrothermal analysis performed in this work parallels the formulation in [8] in most respects, though we have chosen a simpler model where we neglect some effects like radiative heat transfer and variation of the convective heat transfer coefficients and electrical conductivity with temperature. It is possible to extend this work to include these effects without too much additional effort.

The electrical, thermal and mechanical properties used for all the examples in this thesis are as given in

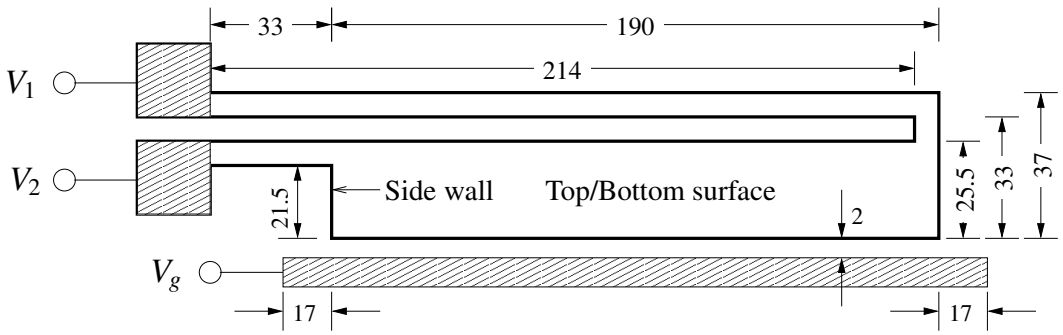

Figure 3.1: Hybrid electrothermomechanical microactuator test setup. All dimensions shown in the figure are in μm. The out-of-plane thickness, t, is 2μm everywhere.

Table 3.1. We have included the variation with temperature of the coefficient of thermal expansion as well as the thermal conductivity. This variation is modeled on the emperical data given in Table 3.2, which is identical to that used in [8].

Parameter	Value
Electrical conductivity of silicon electrode, k_{e_1}	16667 Ω^{-1}m^{-1}
Electrical conductivity of dielectric medium, k_{e_0}	10^{-6} Ω^{-1}m^{-1}
Thermal conductivity, k_t	(see Table 3.2)
Convective heat transfer coefficient	
Top and bottom faces, h_{tb}	130 Wm^{-2}K^{-1}
Side walls, h_s	12,000 Wm^{-2}K^{-1}
Coefficient of linear thermal expansion, α	(see Table 3.2)
Young's modulus, Y	169 GPa
Poisson's ratio, ν	0.3

Table 3.1: Material properties used in the simulation.

3.1.1 Interpolating tabular data

Table 3.2 gives the nonlinear variation of thermal conductivity and the coefficient of thermal expansion with temperature. However, this data is only available at discrete points. To use this data in the model, we need to generate an interpolant that may be evaluated at any value of temperature within the range of the data. We also require the interpolant to be differentiable, since the linearization step of the Newton-Raphson method calls for derivatives of the material parameters with respect to temperature.

To resolve this problem, one option is to linear interpolate the values given in the table. However the derivatives computed from this interpolant will not be very accurate. In order to obtain a smoother function, we apply an exponential fit to the data. We consider a function of the form,

Temperature (K)	k_t (W/(m.K))	α (μm/(m.K))
300	146.4	2.568
400	98.3	3.212
500	73.2	3.594
600	57.5	3.831
700	49.2	3.987
800	41.8	4.099
900	37.6	4.185
1000	34.5	4.258
1100	31.4	4.323
1200	28.2	4.384
1300	27.2	4.442
1400	26.1	4.500
1500	25.1	4.556

Table 3.2: Thermal variation of properties.

$$f(T) = ae^{bT} + ce^{dT}; \tag{3.1}$$

and obtain the parameters a, b, c and d by applying a least-squares fit to the data. Thus, we obtain functional forms for thermal conductivity and coefficient of thermal expansion as given below,

$$k_t(T) = 615.3\exp(-0.006284 \times T) + 64.19\exp(-0.0006563 \times T); \tag{3.2}$$

$$\alpha(T) = 3.776e^{-6}\exp(0.0001257 \times T) - 7.627e^{-6}\exp(-0.005766 \times T); \tag{3.3}$$

3.2 Pull-in behavior in ETM microactuators

To examine the steady-state behaviour of ETM microactuators, we look at the effect of varying the voltages applied on them and its relation to the pull-in instability. The pull-in phenomenon is characteristic of electrostatic actuation, where for voltages above a certain limit, the applied electrostatic force becomes larger than the mechanical restoring force, resulting in the electrodes contacting each other. The lack of a stable solution causes this instability. In order to observe this instability, we take the hybrid microactuator shown in Figure 3.1 and show that by simulating it under three different test conditions, we can simulate each of these actuator types. In each case, the output displacement at the movable tip of the actuator is measured for various values of a parametric voltage that is applied as explained below.

The first test case simulates the classical ETC microactuator configuration, in which $V_1 = 0$, $V_2 = V$

and V_g is allowed to float, where V is the parametric voltage that is varied. This produces a potential gradient and a corresponding electric field inside the silicon structure. The second case models the classical electrostatic actuator by constraining both V_1 and V_2 to V, while V_g is set to zero. In this case, since the electrical conductivity of the double-beam is much larger than the surrounding air, the entire double-beam structure remains at a constant potential and a potential difference is set up with respect to the ground plate, creating an electric field in the region between the two. The third case illustrates the hybrid microactuator model, where both V_1 and V_g are set to zero, while the voltage V is applied to V_2. This is the most general case, where the electric potential varies not only inside the silicon structure but also in the air surrounding it. It is important to note here that in all the cases, the topology of the device is such that the double-beam structure moves downward for all values of the parametric voltage. In other words, the electrostatic and electrothermal actuation both act in the same direction and are additive in nature when applied together, as in the hybrid ETM case. The pure electrothermal and electrostatic actuation cases were independently validated by comparing with results presented in [8] and [13], respectively.

The results of the simulation are shown in Figure 3.2. The potential and temperature profiles for the hybrid actuator with an excitation of 13 volts are as shown in Figure 3.2(a). As expected, we see that the electric potential varies most sharply inside the thin beam, leading to increased heating in that region, causing the device to bend towards the thicker side. In Figure 3.2(b) we plot the pull-in curves for the electrostatic, electrothermal and hybrid actuation. We observe that hybrid actuation demonstrates the pull-in behaviour that is characteristic of electrostatic actuation. Integrating electrostatic and electrothermal actuation produces a larger displacement than each of them individually for the same voltage. Moreover, though electrothermal actuation gives larger displacement for most values of V, the phenomenon of electrostatic pull-in causes the double-beam electrode to snap down onto the ground plate when the displacement is larger than the stable limit. Since there is a potential gradient in one of the electrodes, one might expect the elecrostatic pressure to be lower than that observed in the pure electrostatic case, where the whole double-beam is held at the same value of potential. However, the topology of this device works in our favor. Since the potential gradient is the least in the thick beam, the electric potential in that region does not differ too much from V. As a result, we get almost the same amount of electrostatic actuation along with electrothermal actuation at no extra cost.

The most important point to note is that the final displacement of the hybrid actuator is not merely an additive superposition of electrostatic and electrothermal actuation. Instead, from Figure 3.2(b) we see that there is almost a 25 percent drop in the pull-in voltage. This can be attributed to the fact that electrothermal actuation brings the two electrodes closer, which increases the electrostatic pressure for the

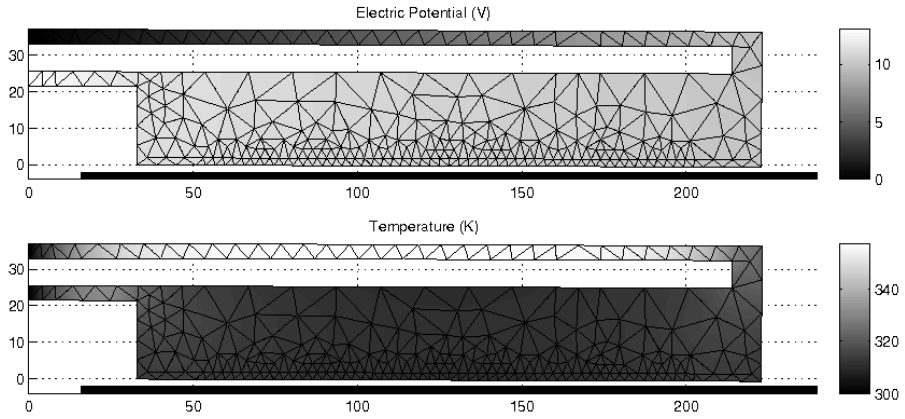

(a) Potential and temperature profiles for the hybrid ETM case (V = 13). Note the potential gradient in the double-beam structure that causes electrothermal actuation in addition to electrostatic traction.

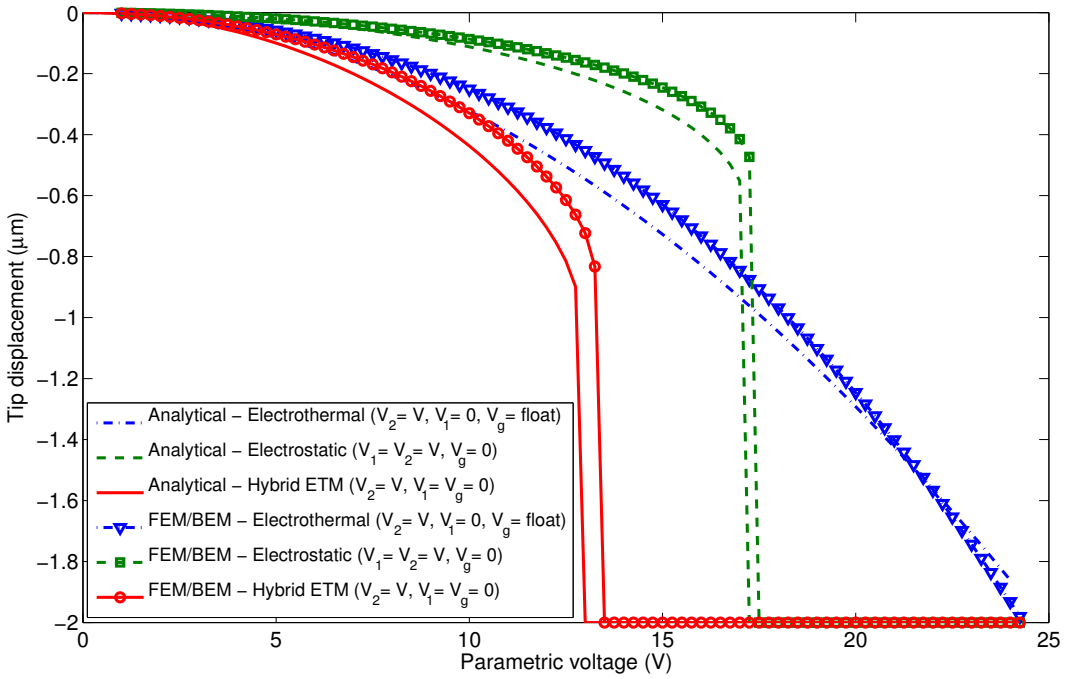

(b) Pull-in curves for different actuator configurations.

Figure 3.2: Hybrid actuator simulation showing (a) the potential and temperature profiles and (b) the pull-in curves that describe the variation of tip displacement with parametric voltage, V.Tip displacement results using the FEM/BEM approach described in Chapter 2, are compared with those from the simplified 1-D analysis performed in Section 3.3.

same value of V and consequently, causes the device to pull-in at a lower voltage. This makes the hybrid actuator ideal for switching applications. The primary benefit is obviously that switching is achieved at a lower voltage than what is required in the electrostatic actuation case. After pull-in has occured, we can shift to pure electrostatic actuation by making V_1 equal to V_2. If this electrostatic voltage is greater than the pull-out voltage for electrostatic actuation, then the double-beam electrode can be held in the pulled-in state using only electrostatic force. Since electrostatic actuation consumes much less power than electrothermal actuation for the same potential difference, this generates various possibilities for efficient standby operation in MEMS switches, when it is required to maintain the device in the deflected (ON) state. Moreover, since the magnitude of electrothermal actuation scales with the dimensions of the device, the mechanical structure can be easily made stiffer if required without adversely affecting the pull-in voltage. This helps to overcome problems related to stiction and improper release of the switch.

3.3 Simplified model

To gain more physical insight into the results obtained in Section 3.2, we look at a simplified analytical model of the hybrid ETM actuator. We look at each of the governing equations presented in Chapter 2 and try to apply reasonable approximations to solve them analytically to the extent possible. The purpose of constructing a simplified model is to approximate the full FEM/BEM model and thus focus only on the important multiphysics couplings. We shall show how the simplified model qualitatively approximates the numerical results obtained in Section 3.2 previously. We shall also examine the shortcomings of this model that are taken care of by the complete model.

3.3.1 Electrical analysis

The actuator consists of 4 regions: the thin arm, the joint at the actuator tip, the thick arm and the flexure, as shown in Figure 3.3(a). To obtain the electric potential in the structure, we consider each of these regions as constant resistances. Since we assume that the medium surrounding the actuator has very low electrical conductivity, we can treat the electrical problem as one where we apply a potential difference across a series combination of the four resistances. This leads to a piecewise-constant electric field in each of the regions and gives a simple expression for the heat source, Q,

$$Q = k_{e_1} E_x^2, \tag{3.4}$$

where E_x is the piece-wise constant value of the electric field along x.

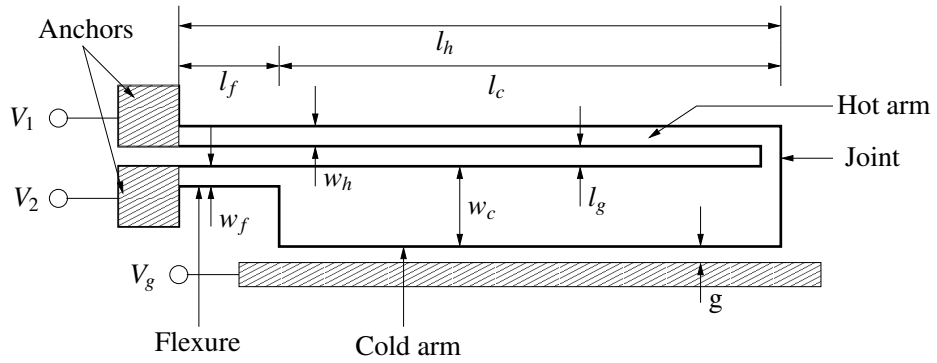

(a) Top view of the hybrid actuator.

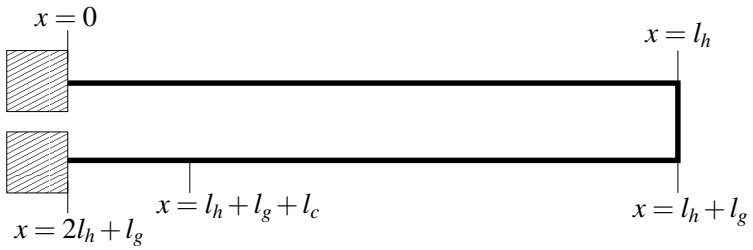

(b) Equivalent 1-D domain for thermal analysis.

Figure 3.3: Model domain for simplified analysis of hybrid ETM actuator. (a) Schematic showing different regions of the actuator and their relevant dimensions. (b)Simplified 1-D domain on which the heat diffusion equation is solved.

3.3.2 Thermal analysis

Similarly, treating the thermal conductivity as a constant, the thermal analysis can be simplified by solving the 1-D heat diffusion equation in the double-beam structure,

$$k_t \frac{d^2T(x)}{dx^2} + Q - \frac{2h_s}{w}(T - T_\infty) = 0, \tag{3.5}$$

with the boundary condition, $T(x) = T_0$, at the device anchors. w is the width at the position x and is equal to w_h, w_c and w_f in the hot arm, cold arm and flexure, respectively. Since the thermal convection from the top/bottom surfaces is small when compared to that from the side walls, it has been neglected in Equation (3.5).

In order to solve this equation analytically, it can be re-written as [25],

$$\frac{d^2\theta(x)}{dx^2} = m^2\theta(x), \tag{3.6}$$
$$\theta(x) = T(x) - T_\theta,$$
$$T_\theta = T_\infty + \frac{Qw}{2h_s} \text{ and}$$
$$m^2 = \frac{2h_s}{k_t w}.$$

Assuming that the temperature field does not vary too much in the joint between the two arms of the double-beam, the solution to Equation (3.6) in the hot arm, the cold arm and the flexure respectively, is given by

$$T_h(x) = T_H + C_{11}\, e^{m_h x} + C_{12}\, e^{-m_h x}, \tag{3.7}$$
$$T_c(x) = T_C + C_{21}\, e^{m_c x} + C_{22}\, e^{-m_c x} \text{ and} \tag{3.8}$$
$$T_f(x) = T_F + C_{31}\, e^{m_f x} + C_{32}\, e^{-m_f x}. \tag{3.9}$$

where $T_h = T_\infty + Qw_h/(2h_s)$, $T_c = T_\infty + Qw_c/(2h_s)$ and $T_f = T_\infty + Qw_f/(2h_s)$. Similarly, m_h, m_c and m_f are given by $m_h = \sqrt{2h_s/(k_t w_h)}$, $m_c = \sqrt{2h_s/(k_t w_c)}$ and $m_f = \sqrt{2h_s/(k_t w_f)}$, respectively. The constants C_{ij} can be solved by substituting the above into Equation (3.6). We apply the boundary conditions at the anchors as well as the conditions of continuity of temperature field and normal heat flux at each of the interfaces between the hot arm, cold arm and flexure, to get a linear system of equations [25]. We assume that the width of the flexure is equal to that of the hot arm, i.e. $w_f = w_h$, and that the length of the cold arm is approximately equal to that of the hot arm, i.e. $l_c \approx l_h$. It can be shown that this system of equations can be solved analytically to obtain an expression for the difference in the average temperatures in the hot and cold arms, $\overline{T_h}$ and $\overline{T_c}$, respectively,

$$\overline{T_h} - \overline{T_c} = \frac{3k_{e_1}(V_2 - V_1)^2(\sqrt{w_c} - \sqrt{w_h})}{l_h w_h \left(l_h/w_h + l_c/w_c + l_f/w_f\right)^2}\sqrt{\frac{k_t}{(2h_s)^3}}, \tag{3.10}$$

where $V_2 - V_1$ is the potential difference applied between the anchors. In deriving this expression, we have used the approximation that $\exp(l_h/m_h), \exp(lc/mc) \gg 1$, which holds quite well for the values used here.

3.3.3 Mechanical analysis

Equation (3.10) can be used to calculate the displacement of the actuator tip, d_t due to electrothermal actuation, using the expression given in [26],

$$d_t = \frac{\alpha \left(\overline{T_h} - \overline{T_c}\right) l_h^2}{2l_g \left(0.7707 + 0.3812(w_h/l_g)^2\right)}, \tag{3.11}$$

where l_g is the gap between the hot and cold arms, as shown in Figure 3.3(a).

The electric field in the dielectric medium is mainly concentrated in the region between the cold arm and the ground plate. Hence, the electrostatic force on the structure can be assumed to be localised on the cold arm and can be neglected everywhere else. The force can be computed by using a parallel-plate approximation to model the electric field between the cold arm and the ground plate, while neglecting fringing fields. Electrostatic force becomes active only when the ground plate is held at some potential and is taken to be zero when the potential of the ground plate is allowed to float. It is proportional to the square of the potential difference between the cold arm and the ground plate. From Section 3.2, we know that the potential in the double-beam structure varies along its length. In this simplified model, we compute the average potential in the cold arm, V_{avg}, and consider the potential difference between the cold arm and the ground plate to be $V_{avg} - V_g$ everywhere. The electrostatic force can then be written as,

$$F_{es} = \frac{\epsilon_0 l_c t (V_{avg} - V_g)^2}{2(g-d)^2}, \tag{3.12}$$

where t is the out-of-plane thickness, g is the gap between the cold arm and the ground plate and d is the displacement of the actuator tip in the direction towards the ground plate. To obtain V_{avg}, we again use the electric potential model, where the potential in the double beam structure is approximated by that in a series combination of resistances. V_{avg} is, therefore, the average potential in the resistance corresponding to the cold arm and is given by,

$$V_{avg} = V_1 + (V_2 - V_1)\frac{l_h/w_h + l_g/w_g + l_c/(2w_c)}{l_h/w_h + l_g/w_g + l_c/w_c + l_f/w_f}. \tag{3.13}$$

Under the condition of static equilibrium, this electrostatic force can be equated to the mechanical restoring force in the deformed double-beam structure to obtain an expression for the displacement of the actuator tip,

$$\frac{\epsilon_0 l_c t (V_{avg} - V_g)^2}{2(g-d)^2} = k_m (d - d_t), \tag{3.14}$$

where k_m is the spring constant of the structure evaluated from Euler-Bernoulli beam theory.

3.3.4 Results

Using this analytical model, we can simulate the three test cases mentioned in Section 3.2, by appropriately setting the values of V_1, V_2 and V_g. In each of the cases, we have a parametric voltage V that is varied and the tip displacement is plotted as a function of this parametric voltage. The results of the simplified analysis are shown in Figure 3.2(b).

It is readily seen that the simplified analysis is able to match the hybrid FEM/BEM analysis for the electrostatic and electrothermal actuation test cases to a resonable degree of accuracy. In both cases, the displacements obtained through the analytical model are greater than the FEM/BEM results for the most part, but are still close in comparison. However, there is a greater degree of mismatch in the hybrid actuation case. One reason for this is that the electrostatic force is taken to be constant all along the cold arm in the analytical model, whereas in reality it will change from one point to the other. Since the displacement varies along the cold arm, the electric field and hence the local electrostatic force is a function of position. In addition, the potential in the cold arm also varies spatially and merely taking the average of the potential in the arm, induces some approximation when calculating electrostatic force. Moreover, since the electrostatic force is nonlinear, small deviations in electrothermal and electrostatic actuation are amplified in the final displacement. The full-blown FEM/BEM analysis is able to take all this into account and is a more accurate model of the actual situation. Nevertheless, the analytical model provides compact expressions for electrothermal and electrostatic actuation, that can be used to gain insight into the qualitative dependence on each of the system parameters.

3.4 Variation of potential gradient

The hybrid actuator framework also allows for the analysis of a variety of potential configurations hitherto not available in conventional actuators. One of the characteristics that distinguishes hybrid ETM actuators, is that the electric potential can vary inside the actuator electrode. This is unlike conventional electrostatic actuators where the electrodes are held at a uniform potential and their boundaries are assumed to be equipotential surfaces. By contrast, when a potential gradient is set up in the electrode, it has two consequences. Firstly, it causes a flow of current, which leads to Joule heating. Secondly, the electrostatic force that acts on the electrode boundaries gets modified.

In the device shown in Figure 3.1, if we ground the bottom plate, keep V_2 fixed and vary V_1 between

0 and V_2, we see the effect of varying potential in the device. We define a parameter, $\lambda = (V_2 - V_1)/V_2$, which is the normalized potential gradient in the electrode. This parameter can be thought of as a means to smoothly interpolate between the latter two configurations discussed in Section 3.2. $\lambda = 0$ corresponds to the condition $V_1 = V_2$, which is identical to the electrostatic case. Similarly, when $\lambda = 1$, it implies that $V_1 = 0$, which corresponds to the hybrid actuator case.

3.4.1 Variation with thermal expansion

Figure 3.4(a) shows the outcome of varying the potential gradient, λ, for different values of V_2. This result naturally follows from the discussion in Chapter 2, where we observe that for any given voltage V_2, the hybrid ETM actuator produces a much larger displacement when compared to the pure electrostatic actuator. It should be noted that varying the potential gradient affects not just the electrothermal expansion alone, but also the electrostatic traction, due to the changing potential field distribution. In any real conducting material, these two effects go hand in hand, because a potential gradient in the electrode that causes the flow of current, also results in a modification of the electric field, and hence the electrostatic traction, at the boundaries.

3.4.2 Variation without thermal expansion

To isolate one effect from the other, we can also look at a fictitious case where electrothermal effects are ignored, by arbitrarily setting the thermal expansion coefficient, α, to be zero. Figure 3.4(b) examines the effect of changing electrostatic traction alone, assuming that there is no thermal expansion. Now we clearly see that by itself, a non-zero potential gradient ($\lambda \neq 0$ or $V_1 \neq V_2$) in the device reduces the electrostatic contribution to the final displacement and results in lower tip displacement. It is the inclusion of thermal effects that is responsible for the marked increase in displacement and the improvement in device performance as seen from the decrease in pull-in voltage in Figure 3.2(b). However, as explained in Section 3.3, it is important to understand the change in electrostatic actuation due to the potential gradient, to accurately predict the pull-in characteristics of the device. The hybrid analysis framework helps to model these unconventional potential configurations with good precision. These results demonstrate the flexibility that hybrid ETM actuation gives, when designing novel devices.

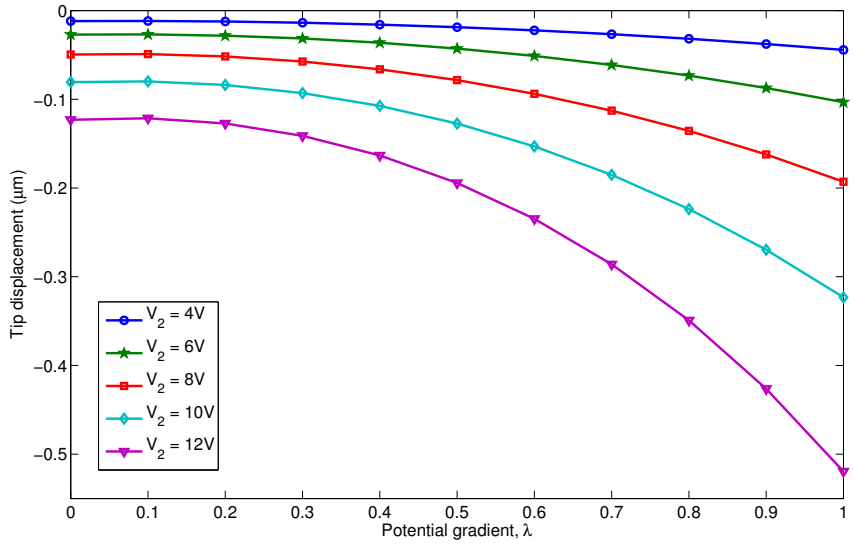

(a) Electrothermal effects included.

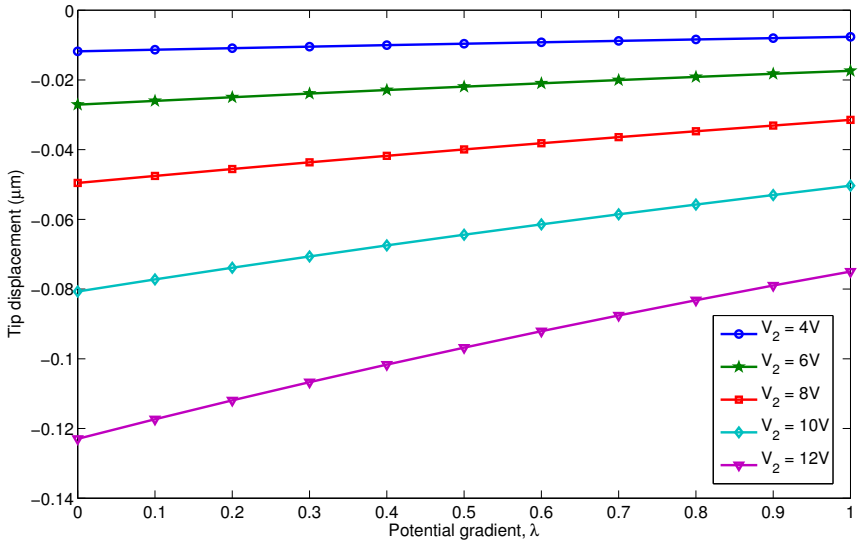

(b) Electrothermal effects not included ($\alpha = 0$).

Figure 3.4: Hybrid actuator with varying potential gradient for different values of V_2.The displacement in both (a) and (b) is almost identical when $\lambda = 0$, the electrostatic case. The effect of setting α to zero is maximum for $\lambda = 1$, where there is maximum electrothermal expansion.

3.5 Bidirectional actuation

Another example that demonstrates the use of multiple potential configurations, is the extension of the hybrid microactuator to produce bidirectional actuation. Both the Guckel microactuator as well as the simple cantilever beam electrostatic microactuator are limited in the sense that their motion is always unidirectional, irrespective of the sign of the potential difference that is applied between the terminals. Bidirectional actuation can be achieved by extending the structure as shown in Figure 3.5. The device shown can be thought of as two double-beam actuators placed facing each other with their tips joined by a short bar. Applying a potential difference between terminals V_1 and V_2 and/or between V_3 and V_4 causes the double-beam structures to bend downwards in the usual manner as seen in the previous examples. Recalling the analogy of resistors in series described in Chapter 2, we note that the same holds in this case as well and the downward motion is because the thin beams undergo greater expansion.

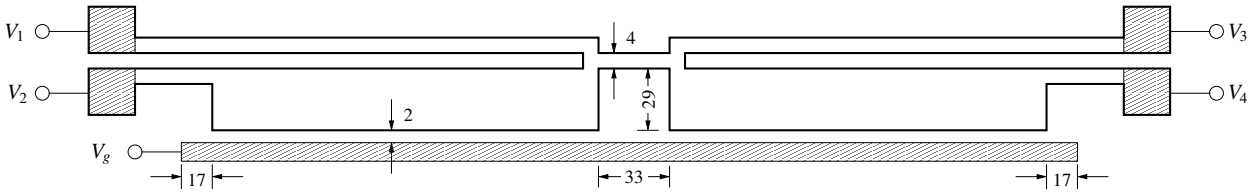

Figure 3.5: Test setup used for bidirectional microactuator simulation. All dimensions mentioned are in μm. Dimensions for the double-beam structures are identical to those given in Figure 3.1. The out-of-plane thickness is 2μm everywhere.

However, applying a potential gradient along the length of the device causes very different behaviour. Now the potential distribution is such that in each double-beam structure, the two beams behave like a pair of resistors connected in parallel. Hence, the electrical power dissipated in each of them is now inversely proportional to their resistance. Consequently the thicker beams, which have a larger cross-sectional area, experience greater thermal expansion, causing the device to now bend upwards. This is clearly seen by comparing the temperature profiles in both cases, as seen in Figure 3.6. Plotting the displacement of the mid-point of the bar connecting the two double-beam structures (see Figure 3.7), we observe that the structure does indeed move in either direction depending on the potential configuration that is applied. We also observe that the device exhibits pull-in behaviour in the downward motion case, due to the electrostatic force that is applied.

The hybrid bidirectional actuation combined with pull-in behaviour is especially useful in switching applications in MEMS. In addition to the advantages of low voltage and low power operation seen in previous examples, the bidirectional operation solves problems due to stiction. As noted earlier, in MEMS switches, stiction occurs when the moving structure sticks to the ground plate due to adhesive forces and the mechanical

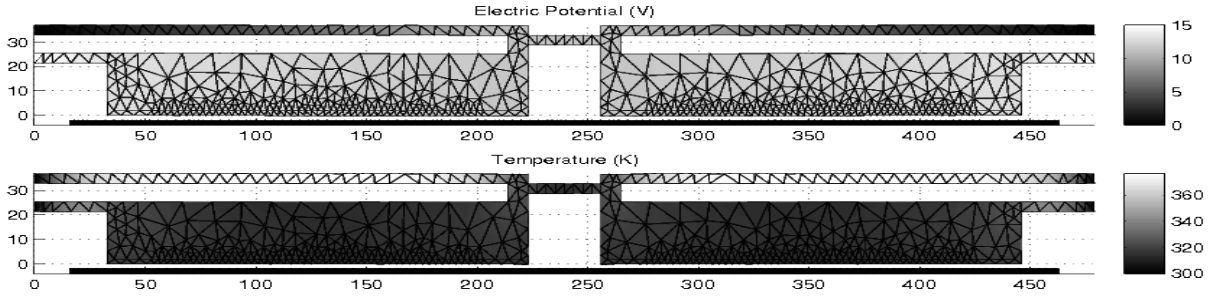

(a) Downward motion ($V_1 = V_3 = V_g = 0; V_2 = V_4 = V$).

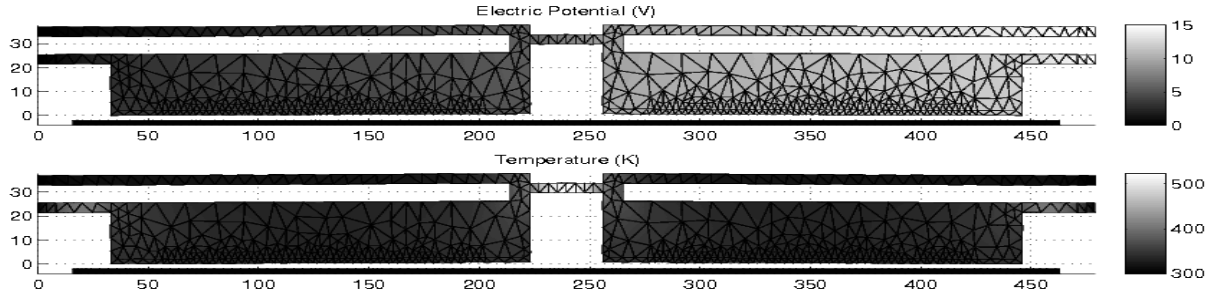

(b) Upward motion ($V_1 = V_2 = 0; V_3 = V_4 = V; V_g = float$).

Figure 3.6: Temperature and potential fields in the bidirectional microactuator for downward and upward motion cases for V = 15V.

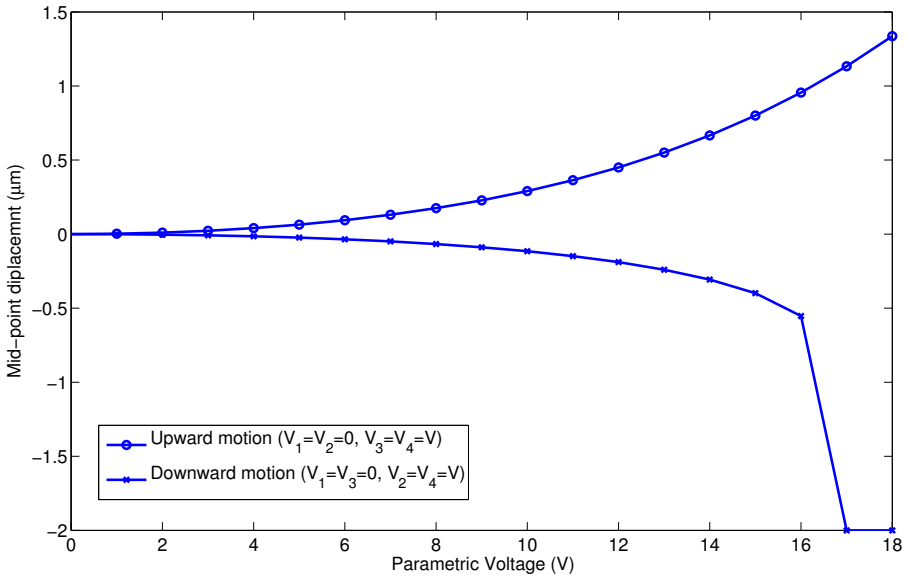

Figure 3.7: Displacement of mid-point of bidirectional actuator, showing how downward and upward motion may be achieved by merely changing the potential boundary conditions.

restoring force in the structure is not strong enough to overcome the adhesion. Having a bidirectional actuator overcomes this problem by generating enough force to surmount the stiction to bring the device back to its original state. Since the direction of operation can be reversed by merely changing the value of electric potential applied to the terminals, this device presents a compact way of implementing a bidirectional switch.

Chapter 4

Conclusions

The work presented in this thesis documents an approach to integrate electrothermal and electrostatic actuation in microelectromechanical systems and thereby combine their advantages. We proposed a novel formulation to model coupled electrothermomechanical microactuators, that takes the current conduction equation that is used to model electrothermal actuators and extended it to describe the electric potential in the electrodes as well as in the dielectric medium between them by assigning a small, fictitious value of conductivity to the exterior medium. We then considered the boundary integral formulation that is popularly used in electrostatic actuation and used it in the generalized current conduction equation to transform the equations in the infinite dielectric medium into integral equations on the boundary of the bodies. This hybrid BIE/Poisson approach preserves the accuracy of the solution and greatly reduces the computational time required for numerical simulation.

A few examples were simulated to demonstrate the capability of the method. We simulated the behaviour of the hybrid double-beam actuator under different voltage boundary conditions. In particular, we demostrated low voltage, low power operation that could be used for switching applications in MEMS. To better understand the behaviour of the hybrid actuator, we developed a simple analytical model for the double-beam ETM actuator. This model yielded qualitatively good results when compared to the solution obtained from the numerical solver. We showed how this simple model gives us a handle into the underlying physics by providing a tool for quickly demonstrating a proof of concept. We also extended the hybrid double-beam actuator towards bidirectional actuation and demonstrated how it may be used to overcome common problems like stiction that occur in MEMS switches.

The idea of integrating different kinds of actuation mechanisms to improve performance has been investigated in the past [3, 6], but only in cases where the different mechanisms are spatially and/or temporally separated. In this research work, we demostrate how efficiency may be improved by proposing a hybrid model for electrothermomechanical actuation that uses electrothermal and electrostatic actuation simultaneously. This hybrid actuation framework readily lends itself to simulating a variety of potential configurations that cannot be analysed using existing ETC and electrostatic actuator models. This formulation also opens up for design and analysis, a whole new class of devices that integrate the two effects.

References

[1] T. Moulton and G. Ananthasuresh, "Micromechanical devices with embedded electro-thermal-compliant actuation," *Sensors and Actuators A: Physical*, vol. 90, pp. 38–48, May 2001.

[2] L. Que, J. Park, and Y. Gianchandani, "Bent-beam electro-thermal actuators for high force applications," in *Proceedings of the Twelfth IEEE International Conference on Micro Electro Mechanical Systems, MEMS '99*, pp. 31–36, Jan 1999.

[3] P. Robert, D. Saias, C. Billard, S. Boret, N. Sillon, C. Maeder-Pachurka, P. Charvet, G. Bouche, P. Ancey, and P. Berruyer, "Integrated RF-MEMS switch based on a combination of thermal and electrostatic actuation," in *Proceedings of the Twelfth International Conference on Solid State Sensors, Actuators and Microsystems*, vol. 2, pp. 1714–1717, Jun 2003.

[4] P. Grant, M. Denhoff, and R. Mansour, "A comparison between RF-MEMS switches and semiconductor switches," in *Proceedings of the 2004 International Conference on MEMS, NANO and Smart Systems*, pp. 515–521, Aug 2004.

[5] P. Sumant, A. Cangellaris, and N. Aluru, "Modeling of dielectric charging in RF-MEMS capacitive switches," *Microwave and Optical technology letters*, vol. 49, pp. 3188–3192, Dec 2007.

[6] I.-J. Cho, T. Song, S.-H. Baek, and E. Yoon, "A low-voltage and low-power RF-MEMS switch actuated by combination of electromagnetic and electrostatic forces," in *Proceedings of the 34th European Microwave Conference*, vol. 3, pp. 1445–8, Oct 2004.

[7] H. Guckel, J. Klein, T. Christenson, K. Skrobis, M. Laudon, and E. Lovell, "Thermo-magnetic metal flexure actuators," in *5th Technical Digest, Solid-State Sensor and Actuator Workshop*, pp. 73–75, Jun 1992.

[8] N. Mankame and G. Ananthasuresh, "Comprehensive thermal modeling and characterization of an electro-thermal-compliant microactuator," *Journal of Micromechanics and Microengineering*, vol. 11, pp. 452–462, Sep 2001.

[9] D. S. Chandrasekharaiah and L. Debnath, *Continuum Mechanics*. Academic Press, 1994.

[10] H. Parkus, *Thermoelasticity*. Blaisdell Publishing Company, New York, 1968.

[11] P. Yarrington and D. E. Carlson, "Successive approximations in nonlinear thermoelasticity," *International Journal of Engineering Science*, vol. 14, pp. 113–125, Jan 1976.

[12] N. Aluru and J. White, "An efficient numerical technique for electromechanical simulation of complicated microelectromechanical structures," *Sensors and Actuators A: Physical*, vol. 58, pp. 1–11, Jan 1997.

[13] S. De and N. R. Aluru, "Full-Lagrangian schemes for dynamic analysis of electrostatic MEMS," *Journal of Microelectromechanical Systems*, vol. 13, pp. 737–758, Oct 2004.

[14] S. De and N. R. Aluru, "Complex nonlinear oscillations in electrostatically actuated microstructures," *Journal of Microelectromechanical Systems*, vol. 15, pp. 355–369, Apr 2006.

[15] S. De and N. R. Aluru, "Coupling of hierarchical fluid models with electrostatic and mechanical models for the dynamic analysis of MEMS," *Journal of Microelectromechanical Systems*, vol. 16, pp. 1705–1719, Jul 2006.

[16] H. A. Haus and J. R. Melcher, *Electromagnetic Fields and Energy*. Prentice Hall, 1989.

[17] M. Jaswon and G. Symm, *Integral Equation Methods in Potential Theory and Elastostatics*. Academic Press, New York, 1977.

[18] F. Shi, P. Ramesh, and S. Mukherjee, "On the application of 2d potential theory to electrostatic simulation," *Communications in Numerical Methods in Engineering*, vol. 11, no. 8, pp. 691–701, 1995.

[19] G. Li and N. Aluru, "A Lagrangian approach for electrostatic analysis of deformable conductors," *Journal of Microelectromechanical Systems*, vol. 11, pp. 245–254, Jun 2002.

[20] G. Li and N. Aluru, "Efficient mixed-domain analysis of electrostatic MEMS," *IEEE Transactions on Computer-Aided Design of Integrated Circuits and Systems*, vol. 22, pp. 1228–1242, Nov 2003.

[21] G. Li and N. Aluru, "Hybrid techniques for electrostatic analysis of nanoelectromechanical systems," *Journal of Applied Physics*, vol. 96, pp. 2221–2231, Aug 2004.

[22] G. Li and N. Aluru, "A Lagrangian approach for quantum-mechanical electrostatic analysis of deformable silicon nanostructures," *Engineering Analysis with Boundary Elements*, vol. 30, pp. 925–939, Nov 2006.

[23] J. Kane, *Boundary Element Analysis in Engineering Continuum Mechanics*. Prentice-Hall, Englewood Cliffs, NJ, Jan 1994.

[24] K. Bathe, *Finite Element Procedures*. Englewood Cliffs, NJ: Prentice-Hall, 1995.

[25] Q.-A. Huang and N. K. S. Lee, "Analysis and design of polysilicon thermal flexure actuator," *Journal of Micromechanics and Microengineering*, vol. 9, pp. 64–70, Mar 1999.

[26] R. W. Johnstone and M. Parameswaran, *An Introduction to Surface-Micromachining*, ch. 12, p. 157. Springer, 2004.